Separating Crystallization Process of P3HT and O-IDTBR to Construct Highly Crystalline Interpenetrating Network with Optimized Vertical Phase Separation

Qiuju Liang, Xuechen Jiao, Ye Yan, Zhiyuan Xie, Guanghao Lu, Jiangang Liu,* and Yanchun Han*

The morphology with the interpenetrating network and optimized vertical phase separation plays a key role in determining the charge transport and collection in polymer:nonfullerene small molecular acceptors (SMAs) solar cells. However, the crystallization of polymer and SMAs usually occurs simultaneously during film-forming, thus interfering with the crystallization process of each other, leading to amorphous film with undesirable lateral and vertical phase separation. The poly(3-hexylthiophene) (P3HT):O-IDTBR blend is selected as a model system, and controlling film-forming kinetics to solve these problems is proposed. Herein, a cosolvent 1,2,4-triclorobenzene (TCB) with selective solubility and a high boiling point is added to the solution, leading to prior crystallization of P3HT and extended film-forming duration. As a result, the crystallinity of both components is enhanced significantly. Meanwhile, the prior crystallization of P3HT induces solid–liquid phase separation, hence rationalizing the formation of the nano-interpenetrating network. Moreover, the surface energy drives O-IDTBR to enrich near the cathode and P3HT to migrate to the anode. Consequently, a highly crystalline nano-interpenetrating network with proper vertical phase separation is obtained. The optimal morphology improves charge transport and suppresses bimolecular recombination, boosting the power conversion efficiency from 4.45% to 7.18%, which is the highest performance in P3HT-based binary nonfullerene solar cells.

1. Introduction

Solution-processed nonfullerene solar cells composed of binary blend of a polymeric electron donor and a nonfullerene small molecular acceptors (SMAs) have attracted increasing attention due to their advantages of light absorption tunability, semi-transparency, and flexibility.[1–3] With the development of device structure, interface engineering, material design, and morphology control, impressive power conversion efficiencies (PCEs) have surpassed 14%.[4–6] The morphology of the active layer plays a crucial role in determining the PCE of devices since it is closely related to the photophysical process.[7,8] The ideal morphology of active layers should comprise donor and acceptor materials, which form bicontinuous crystalline networks of 10–20 nm domain size with large interfacial mixed phase, guaranteeing efficient exciton separation, carrier transport, and collection.[9–11]

To achieve the bicontinuous network, the ratio and miscibility between donor and acceptor should be elaborately selected, and it is believed that the optimum composition for forming bicontinuous network should be near the hypoeutectic point.[12–14] For a given set of materials, the donor and acceptor with improved crystalline phases usually facilitate carrier transport.[15] However, blend films are usually kinetically frozen away from thermodynamic stable states during the rapid solvent evaporation of the solution, resulting in low crystallinity. For many polymer:fullerene blends, various postannealing methods, such as thermal annealing and solvent vapor annealing, have been successfully applied to drive the blend systems closer to the thermodynamic stable state.[16–18] The posting annealing should promote the conformation transition of polymers and the molecular diffusion of fullerenes, and facilitate the process of crystallization. Therefore, the thermal annealing temperature should be above the glass transition temperature (T_g) of the polymer, while the solvent used in solvent vapor annealing process should have a certain solubility for the donor and/or acceptor.[19,20]

As we know, the shape of fullerenes is cage like, which facilitates its diffusion and electronic coupling with each other, thus easily forms microcrystals during post annealing process.[21] Nevertheless, there are significant differences between

Dr. Q. Liang, Dr. Y. Yan, Prof. Z. Xie, Dr. J. Liu, Prof. Y. Han
State Key Laboratory of Polymer Physics and Chemistry
Changchun Institute of Applied Chemistry
Chinese Academy of Sciences
5625 Renmin Street, Changchun 130022, P. R. China
E-mail: niitawh@ciac.ac.cn; ychan@ciac.ac.cn
Dr. X. Jiao
Australian Synchrotron
Clayton, Victoria 3168, Australia
Prof. G. Lu
Frontier Institute of Science and Technology
Xi'an Jiaotong University
Xi'an 710054, P. R. China

The ORCID identification number(s) for the author(s) of this article can be found under https://doi.org/10.1002/adfm.201807591.

fullerene and SMAs. SMAs, such as 3,9-bis(2-methylene-(3-(1,1-dicyano-methylene)-indanone))-5,5,11,11-tetrakis(4-hexylpheny)-dithieno[2,3-d:2′,3′-d′]-s-indaceno[1,2-b:5,6-b′]-dithiophene (ITIC) and (Z)-5-{[5-(15-{5-[(Z)-(3-ethyl-4-oxo-2-thioxo-1,3-thiazolidin-5-ylidene)methyl]-8-thia-7.9-diazabicyclo[4.3.0] nona-1(9),2,4,6- tetraen-2-yl]-9,9,18,18-tetrakis(2-ethylhexyl)-5.14-dithiapentacyclo[10.6.0.0³,¹⁰.0⁴,⁸.0¹³,¹⁷]octadeca-1(12),2,4(8),6,10,13(17),15-heptaen-6-yl]-8-thia-7.9-diazabicyclo[4.3.0]nona-1(9),2,4,6-tetraen-2-yl]methylidene}-3-ethyl-2-thioxo-1,3-thiazolidin-4-one (EH-IDTBR), have planar structure, large molecular size, which inhibits molecular diffusion. Moreover, the strong electronic coupling is only expected for molecules oriented with their π systems parallel to each other, leading to weak driving force for aggregation.[1,22,23] Hence, when blended with donor materials, SMAs exhibits weak crystallinity, even after postannealing process.[24] Taking poly(3-hexylthiophene) (P3HT): (5Z, 5′Z)-5,5′-((7,7′-(4,4,9,9-tetraoctyl-4,9-dihydro-s-indaceno[1,2-b:5,6-b′]dithiophene-2,7-diyl)bis(benzo [c][1,2,5]thiadiazole7,4diyl)) bis(methanylylidene)) bis(3-ethyl-2-thioxothiazolidin-4-one) (O-IDTBR) blend system for instance, the highest reported efficiency of 6.4% for P3HT-based nonfullerene devices is achieved after thermal annealing (10 min at 130 °C).[22] However, thermal annealing mainly improved the crystallinity of P3HT, while the crystallinity of O-IDTBR is still low. As a result, the electron mobility is several orders lower than the hole mobility, resulting in a low fill factor (FF), only 0.6, which is lower than those of their fullerene counterparts.[25] Therefore, it is necessary to find effective approaches to enhance the crystallinity of SMAs to further improve the device performance.

Strengthening the interaction of SMAs through molecular tailoring, i.e., reducing the steric hindrance or introducing substituents with strong interaction, is an efficient way to increase the ordered molecular packing.[26,27] The crystallinity of SMAs could be enhanced by lowering the miscibility between polymer and SMAs as well.[13] Recently, researchers have found the crystallinity of polymer:fullerene blends could be optimized through regulating film-forming kinetics.[28,29] The in situ study revealed that the donor and acceptor crystallizing at different stages during film-forming process is beneficial for their nucleation and crystal growth.[30,31] The related work has given us much inspiration that whether it is effective to enhance the crystallinity of SMAs. However, to the best of our knowledge, few works focused on film-forming kinetics in polymer:SMA blend system has been done. Therefore, it is urgent to fully understand the characteristics of film-forming kinetics and construct the relationship of film-forming kinetics, morphology, and photophysical process in polymer:SMA blend system.

In this work, we elucidated the fundamental correlations of film-forming process, nanomorphology of the active layer and device performance in P3HT:O-IDTBR blend. We chose high boiling point 1,2,4-trichlorobenzene (TCB) with selective solubility for O-IDTBR as a cosolvent to separate the crystallization process of P3HT and O-IDTBR, inhibiting the interference between each other during crystallization. The film-forming process is prolonged, permitting molecule diffusion in both lateral and vertical direction. Hence, the crystallinity, lateral and vertical phase separation of the blend film are optimized simultaneously. The morphology is beneficial for the carrier transport and extraction, suppressing the bimolecular recombination, which leads to a high PCE of 7.18% with FF of 0.70. Intriguingly, this FF reaches the highest value among fullerene-free P3HT-based devices, and even higher than the FF of 0.68 in the record-efficient P3HT:PC$_{61}$BM organic solar cells (OSCs). Moreover, the PCE is the highest efficiency of OSCs using the P3HT donor and nonfullerene acceptors.

2. Results and Discussion

Here, the relationship among film-forming kinetics, film morphology, and device performances is systematically investigated. We added TCB as cosolvent into chlorobenzene (CB) to control the film-forming process and optimize the film morphology of P3HT:O-IDTBR blends. The optimum content of TCB is 2.0% in volume ratio as shown in Table S1 (Supporting Information), thus we discuss the morphology and device performance of the film fabricated with 2.0% TCB in volume ratio in detail in the following text unless otherwise stated. Owing to the modified film-forming kinetics after adding TCB, the crystallinity, lateral and vertical phase separation are optimized, resulting in the highest device efficiency of 7.18% for binary P3HT-based fullerene-free devices. In addition, the selection criteria for effective cosolvent in nonfullerene blend systems are discussed as well.

2.1. Regulating the Film-Forming Kinetics

Film-forming kinetics has profound impacts on the molecule orientation, crystallinity, and phase separation structure of films. It can be characterized by in situ grazing incidence X-ray diffraction (GIXD), grazing incidence small-angle X-ray scattering (GISAXS), and so on.[32] These in situ technologies have tremendously advanced our understanding of bulk-heterojunction (BHJ) structure evolution in film-forming process. However, in situ GIXD requires relative high crystallinity of both donor and acceptor, and in situ GISAXS requires obvious contrast between donor and acceptor. To augment the toolkit for in situ measurements, the UV–vis spectroscopy as an in situ measurement technique has been developed.[33,34] According to the theoretical work by Spano, it enabled the quantification of crystallinity for semicrystalline materials from UV–vis spectra by relating the ordered aggregation to optoelectronic coupling between molecules. Hence, it is possible to characterize the film-forming kinetics in blend systems during solution processing by evaluating the variations of UV–vis spectra.[35,36]

Here, we used the UV–vis spectra to reveal the impacts of TCB on film-forming kinetics by tracking the UV–vis absorption intensity of both donor and acceptor during film-forming process. According to the UV–vis spectra of neat P3HT and O-IDTBR solution and films (**Figure 1**A,B), the absorption peaks at ≈505, 550, and 605 nm corresponds to the ordered aggregation of P3HT, and the signal at ≈700 nm originates from intermolecular ordered packing of O-IDTBR.[22] We recorded the evolution of absorption intensity at ≈550 and 700 nm for blend films to monitor the crystallization kinetics of P3HT:O-IDTBR blend system in our experiment. As shown
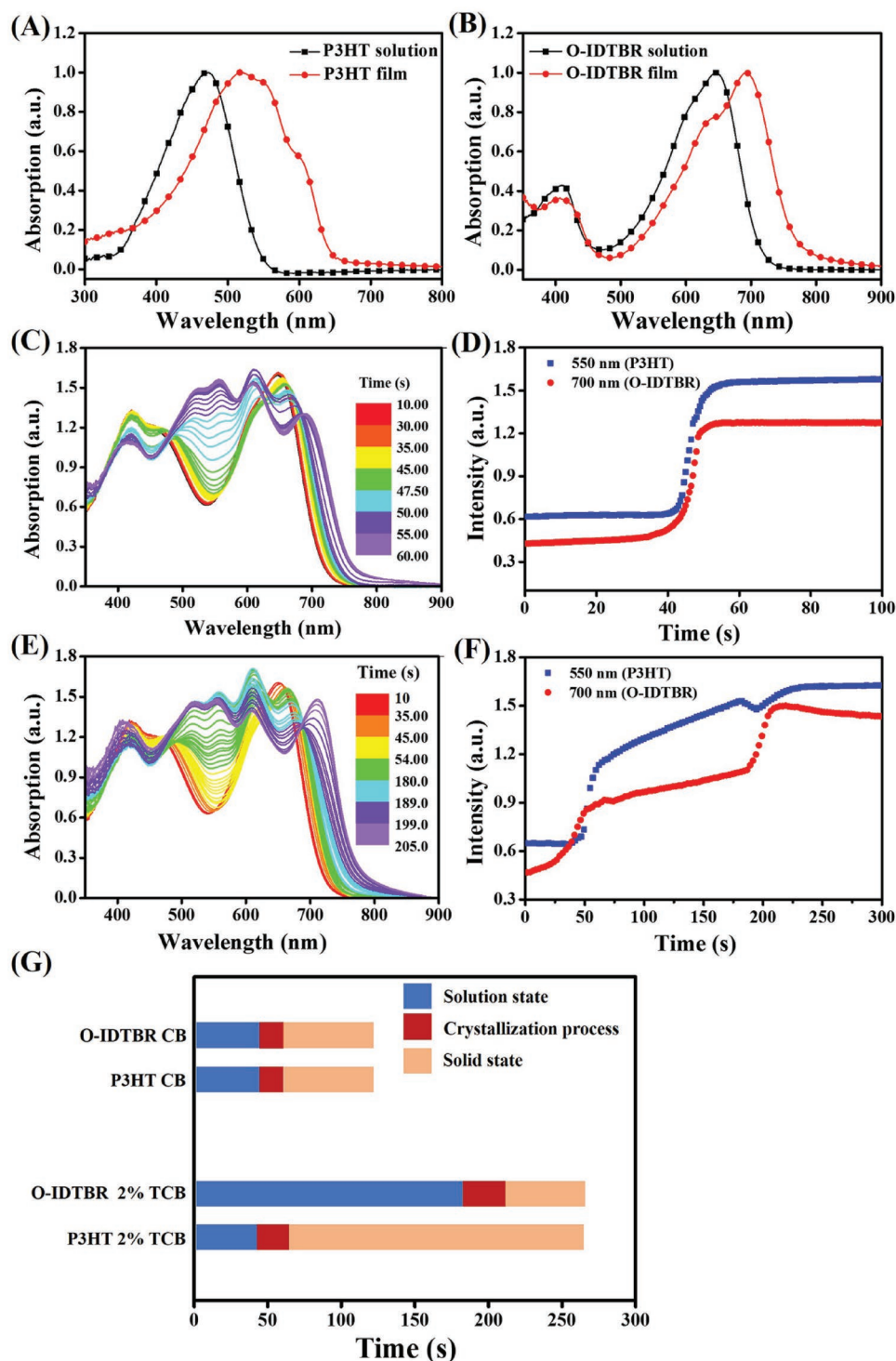
Figure 1. A,B) The UV–vis absorption of P3HT and O-IDTBR solution and film. The UV–vis absorption spectra at different time and the evolution of absorption intensity at 550 and 700 nm during film drying processed without C,D) TCB with E,F) TCB. The abridged graph of film-forming process without and with G) TCB.

in Figure 1C,E, the absorption spectra of film-forming process without TCB and with TCB are characterized. According to these spectra, the crystallization kinetics are identified by plotting the peak intensities of P3HT and O-IDTBR versus time as shown in Figure 1D,F.

As shown in Figure 1D, for the film-forming process without TCB, three different stages were observed. During stage I (0–40 s, dissolved state), P3HT and O-IDTBR remained well dissolved, and no obvious variation of peak intensity was observed. During stage II (40–50 s, crystallization process), as the

**ADVANCED
SCIENCE NEWS**

www.advancedsciencenews.com

**ADVANCED
FUNCTIONAL
MATERIALS**

www.afm-journal.de

solvent continues to evaporate, P3HT and O-IDTBR hit their solubility limits in CB almost at the same time (about 65 and 73 mg mL^{-1}, respectively), followed by the crystallization process, as signaled by the sudden increases of the absorption peak. In this stage, the precipitation of P3HT and O-IDTBR occurred simultaneously. As a result, it was difficult to form pure P3HT phase and O-IDTBR phase. In addition, the crystallization process, i.e., stage II, was relatively short (last about 10 s), thus could not provide enough time for molecular self-organization. During stage III, once the solvent volatilizes completely, the movements of solutes are significantly suppressed, thus the crystallization process comes to an end, and no more P3HT or O-IDTBR crystallites form or grow signaled by the plateau of the absorption peak intensity.

The film-forming process of blend system with TCB also consists of three stages as shown in Figure 1F. The changing tendency of absorption intensity for blend system with TCB is similar to that of blend system without TCB during stage I and stage III. However, there are significant changes in step II. Due to the faster evaporation rate of CB compared to TCB, in early stage II (about 40–50 s), as the evaporation of CB went on, P3HT started to nucleate and grow. Thus, its absorption intensity increased, which was almost the same as the final intensity, indicating the self-organization of P3HT chains has been nearly complete. During the late stage II (about 60–210 s), the residual TCB would further act as plasticizer for the P3HT phase, and thus allowed an extended time period, over which the local adjustment of P3HT chains took place, causing a slight increase of absorption intensity. However, the aggregating behavior of O-IDTBR is different from that of P3HT in stage II. In early stage II (35–50 s), only a small portion of O-IDTBR aggregated and formed crystal nucleus, while most of O-IDTBR still dispersed in the solvent owing to a higher solubility in TCB (124 mg mL^{-1}). As the evaporation of TCB, once O-IDTBR approaches the solubility in TCB, the crystal growth of O-IDTBR starts, which can be confirmed by the rapid enhancement of O-IDTBR absorption intensity (180–210 s). According to these data, it is obvious that the crystallization processes of P3HT and O-IDTBR are separated and the duration of crystallization is also prolonged after adding TCB. This change is believed to be caused by the film-forming kinetics, since the addition of TCB does not affect the aggregating behavior of both P3HT and O-IDTBR in solution, which could be confirmed by the UV–vis spectra of solutions without and with TCB (Figure S2, Supporting Information). We also studied the influence of content of TCB on the film-forming kinetics. Increasing the amount of TCB can further prolong the duration of crystallization and separate the crystallization process more completely as shown in Figure S3 (Supporting Information).

We summarized the main stages in film-forming process without and with TCB mentioned above in Figure 1G, and the different stages are color coded to guide the eye. Two significant differences are observed. First, the crystal growth processes of P3HT and O-IDTBR occurred simultaneously in the blend system without TCB, while in the blend system with TCB, the crystal growth process of P3HT and O-IDTBR occurred at different stages. Second, the duration of crystallization for P3HT and O-IDTBR was extended from 10 to 20 and 30 s, respectively, after adding TCB. The separated crystallization process

and prolonged duration of crystallization must have significant influence on the crystallinity, lateral and vertical phase separation of blend films, and we will discuss it in the following.

2.2. Enhanced Crystallinity of both P3HT and O-IDTBR

GIWAXS measurements were performed to assess the molecular packing and crystal texture. As shown in **Figure 2**AB, the neat P3HT films fabricated without and with TCB exhibit obvious lamellar staking signals (h 0 0) along out-of-plane (OOP) direction and π–π staking signal (010) along in-plane (IP) direction, suggesting that P3HT crystallites adopt edge-on orientation with respect to the substrate. After adding TCB, the crystallinity of P3HT film is slightly enhanced, confirmed by the increased (010) peak intensity along the IP direction (Figure 2C). Furthermore, P3HT crystallites become more edge-on after adding TCB, as evidenced by the stronger pole figure intensity around low pole angle (Figure S4A, Supporting Information). O-IDTBR crystallites adopt face-on orientation evidenced by the simultaneous appearance of (100) lamellar stacking signals along the IP direction and π–π staking signals along OOP direction as shown in Figure 2D,E. After adding TCB, the (100) peak shifts from $q = 0.348$ Å^{-1} ($d = 18.05$ Å) to $q = 0.355$ Å^{-1} ($d = 17.69$ Å) as shown in Figure 2F, which suggests an enhanced intermolecular interaction. Besides, TCB reduces the degree of random orientation of O-IDTBR as shown in Figure S4B (Supporting Information).

For the P3HT:O-IDTBR film, the lamellar peaks from P3HT persist, and its diffraction gets stronger after adding TCB as shown in Figure 2G,H, indicating the enhanced crystallinity of P3HT. Furthermore, the lamellar stacking distance is slightly reduced since the peak shifts from $q = 0.362$ Å^{-1} ($d = 17.35$ Å) to $q = 0.365$ Å^{-1} ($d = 17.21$ Å), shown in **Table 1**. The OOP and IP linecuts of the blend films are shown in Figure 2I, and the multi-peak fitting results are shown in Figure S4D,E (Supporting Information). Using the fitting curve, the coherence length of P3HT along (h 0 0) can be calculated from the Scherrer equation and it increases from 116.3 to 128.2 Å (Table 1). The diffraction peaks of O-IDTBR of blend film shows an obvious variation, which can be clearly distinguished by the close-up views in the upper right corner of Figure 2G,H. First, the intensity of both the (100) and (010) diffractions gets enhanced, and the crystal size also increases from 184.7 to 330.5 Å (Table 1), which indicates the enhanced crystallinity of O-IDTBR. In addition, the diffraction becomes a sharp arc (Figure 2E), indicating more O-IDTBR crystallites adopt face-on orientation. The UV–vis absorption spectra also identify the enhanced crystallinity of P3HT and O-IDTBR because the absorption at 505, 550, 600, and 700 nm of the blend film prepared with TCB is much stronger than that of without TCB as shown in Figure S5 (Supporting Information).

Combined with film-forming kinetics, the reason that adding TCB enhanced the crystallinity of blend film was proposed. When the film processed from the solution without TCB, the crystallization of P3HT and O-IDTBR occurs simultaneously. As a result, the whole system is quenched into a mixed state, thus O-IDTBR molecules disperse in P3HT chains,
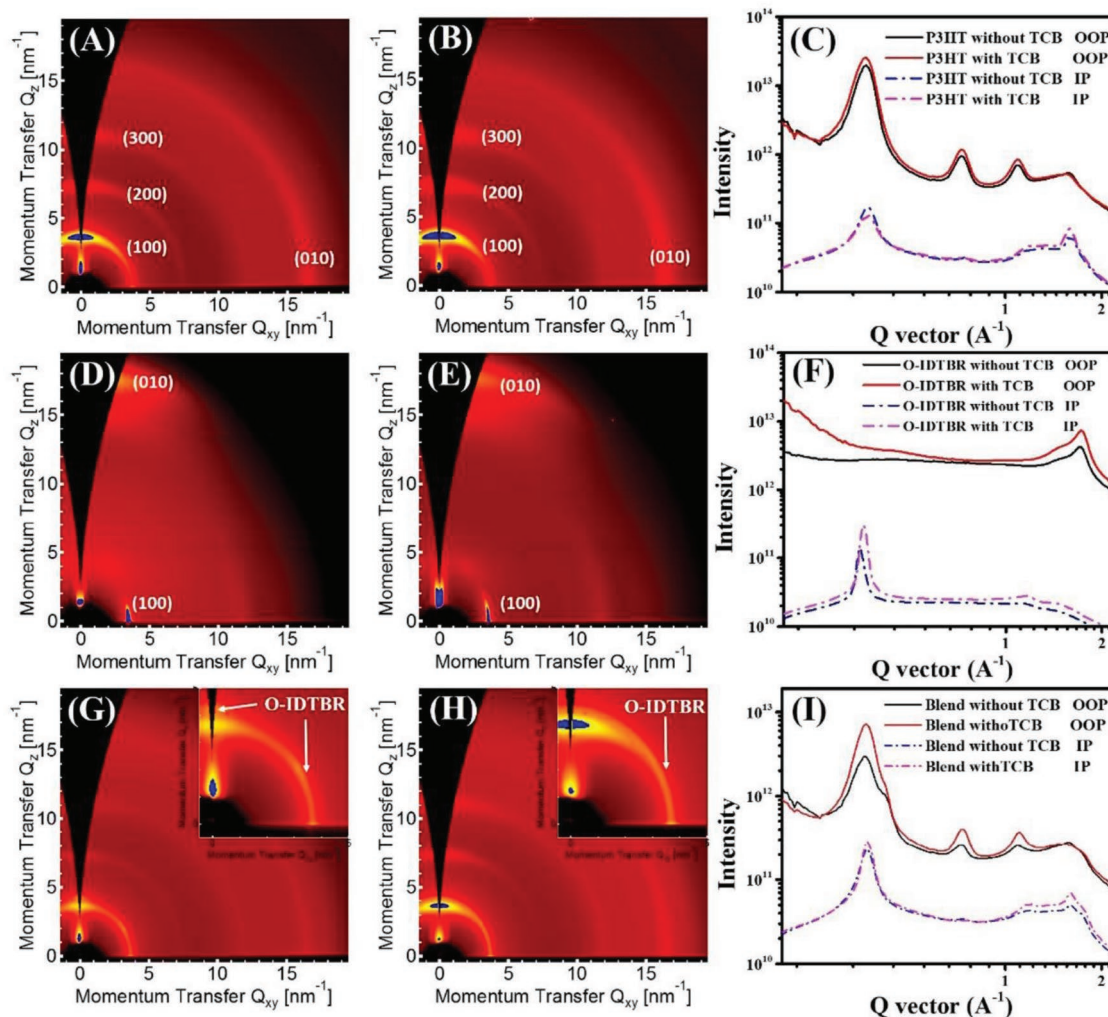
Figure 2. The GIWAXS diffraction patterns of neat P3HT films and O-IDTBR neat films fabricated A,B) without and D,E) with TCB. The GIWAXS diffraction patterns of P3HT:O-IDTBR blend films fabricated G) without and H) with TCB. C,F,I) The OOP and IP linecuts of neat P3HT films, O-IDTBR films and P3HT:O-IDTBR blend films.

interrupting the ordered aggregation of both P3HT chains and O-IDTRB. Moreover, the crystallization process is relatively short. As we know, the movements of both P3HT and O-IDTBR molecules in the solution become suppressed with ongoing solvent evaporation since the solvent molecules act as plasticizer to increase the molecular diffusion. Thus, the crystallinity is low because there is no sufficient time for mass transport and chain rearrangement.[12,37] While after adding TCB, the crystallization of P3HT and O-IDTBR occurs at different time period, which tends to form relative pure phases and can reduce the interference of each other during crystallization process. This phenomenon was also observed in polymer:fullerene blend systems.[38] In addition, the duration of crystallization of both P3HT and O-IDTBR is prolonged due to the lower evaporation rate of TCB, thus P3HT and O-IDTBR have enough time for regulating the chain conformation and diffusion, which further facilitates the blend system to close its equilibrium state, i.e., forming crystals in proper orientation.

2.3. Improved Lateral Phase Separation Structure

Here, the morphology of P3HT:O-IDTBR blend films was characterized by atomic force microscopy (AFM) and transmission electron microscopy (TEM). As shown in **Figure 3**A, the film processed without TCB shows an overlay of large spherical domains
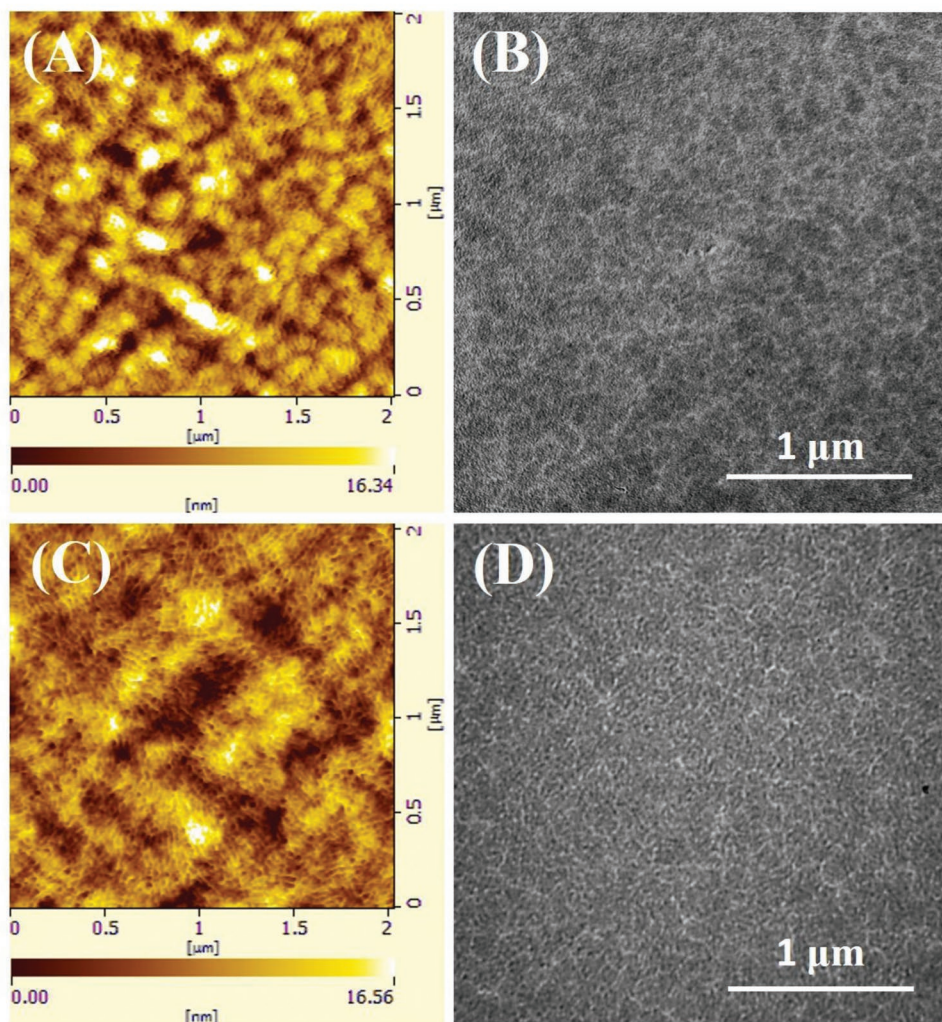
Table 1. The diffraction data of GIWAXS.

	q location [Å^{-1}]	d spacing [Å]	FWHM [Å^{-1}]	Coherence length [Å]
Peak$_{P3HT}$ without TCB	0.362	17.35	0.054	116.3
Peak$_{O\text{-}IDTBR}$ without TCB	0.421	19.42	0.034	187.7
Peak$_{P3HT}$ with TCB	0.365	17.21	0.049	128.2
Peak$_{O\text{-}IDTBR}$ with TCB	0.421	14.92	0.019	330.5

**ADVANCED
SCIENCE NEWS**
www.advancedsciencenews.com

*ADVANCED
FUNCTIONAL
MATERIALS*
www.afm-journal.de

Figure 3. The AFM and TEM images of films prepared without A,B) TCB, films prepared with C,D) TCB.

(>300 nm) and fibrillar structure, and displays a root-meat-square roughness (RMS) of 5.35 nm. While after adding TCB, more nanofibers begin to emerge, thus forms interpenetrating network (Figure 3C). The domain size decreases as well, which can be estimated from the reduced RMS value of 2.48 nm. The TEM images are consistent with the AFM results (Figure 3B), in which the film prepared without TCB shows lager phase separation with grain-like aggregates, while the domain size decreases and the fibrillar structure becomes more obvious after the addition of TCB (Figure 3D). The morphology of other TCB contents are shown in Figure S6 (Supporting Information), which further indicates that the addition of TCB promotes the formation of interpenetrating network. If excessive TCB exists, large domains form and the interpenetrating structure is destroyed again (AFM and TEM images of other amount of TCB are shown in Figure S6, Supporting Information).

The different morphology is attributed to the film-forming kinetics. As we know, before the solvent completely evaporates, either liquid–liquid (L–L) or liquid–solid (L–S) phase separation may occur.[30] For the film prepared without TCB, P3HT, and O-IDTBR tend to precipitate at the same time, leading

to continuous fluctuations in composition, and L–L phase separation occurs. The mixture enters the spinodal region of the ternary phase diagram, resulting in large P3HT-rich and O-IDTBR-rich domains with low purity. After adding TCB, the aggregation of P3HT is prior to that of O-IDTBR. The aggregation of P3HT induces the L–S phase separation before L–L phase separation occurs, avoiding large phase separation structure. P3HT forms crystalline nanoscale network, which helps to construct nano-interpenetrating network with high phase purity (the phase purity was characterized by the fluorescence spectra as shown in Figure S7, Supporting Information).

The carrier mobility also can be used to judge whether the blend films form interpenetrating network. The charge-carrier mobility was characterized by using the space-charge-limited current (SCLC) method (as shown in **Figure 4**) and the obtained data are summarized in **Table 2**. The hole-only and electron-only device structures are ITO/PEDOT:PSS/active layer/MoO$_3$/AL and ZnO/active layer/PFNBr/Al, respectively. For the device fabricated without TCB, the value of μ_h and μ_e is 4.98×10^{-4} and 7.32×10^{-6} cm^2 V^{-1} s^{-1}, respectively. The carrier mobility is relatively low, especially the electron mobility, and the charge
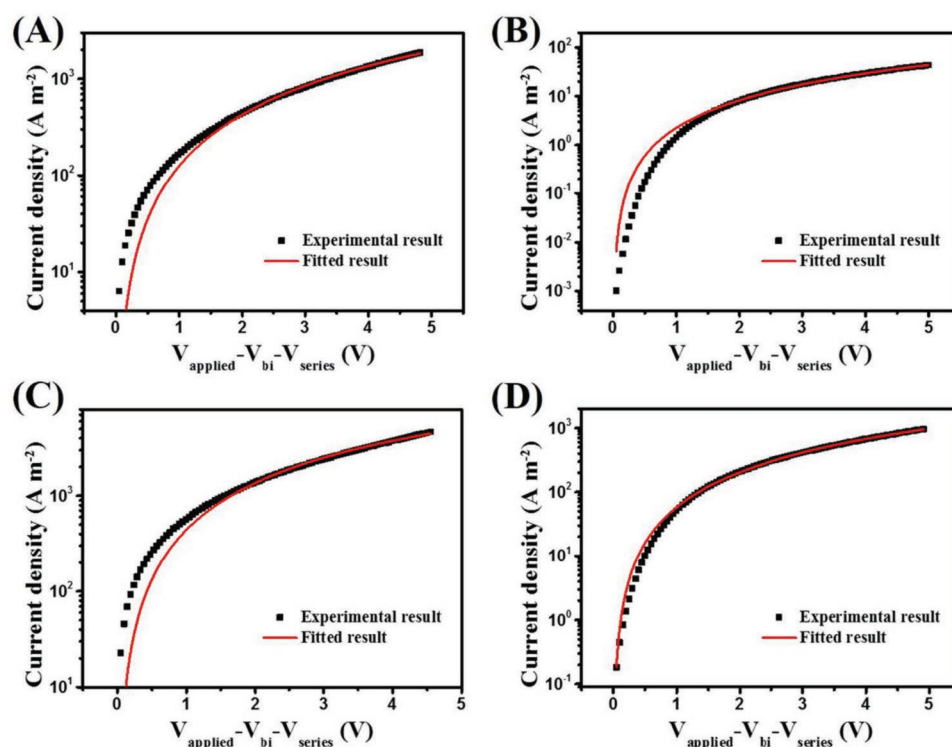
Figure 4. Space-charge-limited J–V characteristics in dark for hole-only devices based on P3HT:O-IDTBR blend film fabricated without A) TCB and with B) TCB. Space-charge-limited J–V characteristics in dark for electron-only devices of P3HT:O-IDTBR blend film fabricated without C) TCB and with D) TCB.

transport is unbalanced ($\mu_h/\mu_e = 68$), which results from the low crystallinity and discontinuous pathways. For the device fabricated with TCB, the hole and electron mobility increase to 2.21×10^{-3} and 2.13×10^{-4} cm^2 V^{-1} s^{-1}, respectively. The electron mobility increases nearly 30 times and a lower μ_h/μ_e ratio is obtained as well. The balanced hole and electron transport with high mobility indicates the formation of crystalline interpenetrating network.

2.4. Optimized Vertical Phase Separation Structure

The vertical phase separation was investigated through film-depth-dependent light absorption spectra, which is an emerging technique to study the composition change in the vertical direction.[39] The film is incrementally etched by the low-pressure (<20 Pa) oxygen plasma without damage of material below the etched surface. The etched film was characterized by a light absorption spectrometer and the film-depth-dependent light absorption spectra could be obtained. Through these spectra, we compared the transmission light intensity of the entire film with the one of the etched films. The derivation corresponds

to the change of light absorption at each wavelength during etching, which can be used as the light absorption for each corresponding sublayer (this method has been described in detail in other literature).[38,39] Here, the light reflection is neglected. The sublayer light-harvesting properties of the films are shown in **Figure 5**A,B. Through these spectra, P3HT contents along vertical direction were obtained as shown in Figure 5C. For the film prepared without TCB, the content of P3HT at the surface (0–20 nm) is 89%, while it remains nearly 50% in the other sublayers (40–180 nm). However, for the film prepared with TCB, the content of P3HT gradually decreases from 96% to 42% from surface to bottom of the film. By comparing these two sets of data, it indicates that P3HT molecules tend to aggregate on the top of the film and the O-IDTBR is prone to sink at the bottom of the film after adding TCB. That is to say, the donor enriches at the anode and the acceptor accumulates at the cathode after adding TCB, which is beneficial for reducing the bimolecular recombination for the ITO/ZnO/P3HT:O-IDTBR/MoO$_3$/Al device structure.

To illustrate the changes of vertical phase separation, we evaluated the surface energy of the P3HT and O-IDTBR by calculating the surface tensions based on contact

Table 2. The carrier mobilities and device parameters of P3HT:O-IDTBR processed without and with TCB.

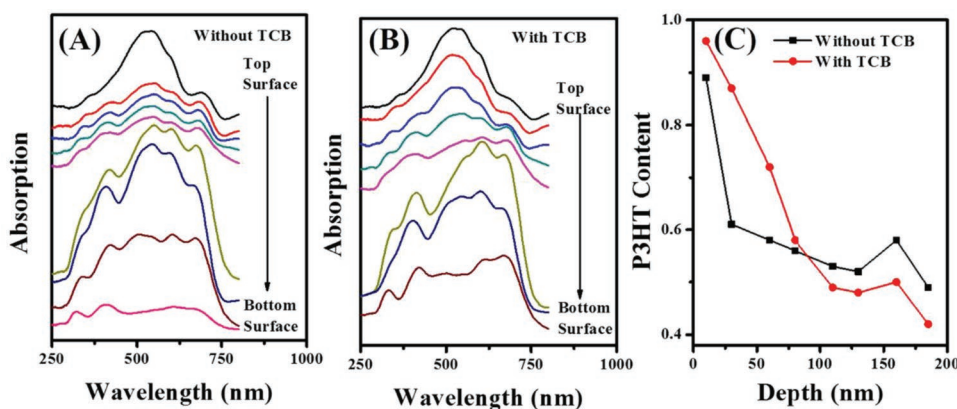| Conditions	Hole mobility [cm^2 V^{-1} s^{-1}]	Electron mobility [cm^2 V^{-1} s^{-1}]	μ_h/μ_e	V_{oc} [V]	J_{sc} [mA cm^{-2}]	FF	PCE [%]
Without TCB	4.98×10^{-4}	7.32×10^{-4}	68	0.77	8.81	0.64	4.45 (4.25 ± 0.20)
With TCB	2.21×10^{-3}	2.13×10^{-4}	10	0.76	13.49	0.70	7.18 (7.00 ± 0.17)

Figure 5. Film-depth-dependent light absorption spectra of P3HT:O-IDTBR blends prepared A) without TCB and B) with TCB. The spectra were vertically shifted and rescaled for clarity. The sublayer thickness for each spectrum is ≈20 ± 4 nm. Top and bottom surfaces represent P3HT:O-IDTBR/MoO₃ and ZnO/P3HT:O-IDTBR interfaces, respectively. C) The calculated weight ratio of P3HT along the vertical direction from top (0 nm) to bottom surfaces (200 nm).

angle measurements. The contact angles of two different solvents (water and glycerol) on the neat films were measured and compared. As shown in Figure S8 (Supporting Information), P3HT film shows a higher water contact angle and is more hydrophobic than O-IDTBR film. The same trend also can be observed for glycerol contact angles. According to the contact angle data, the surface tensions (γ) was calculated by Wu model. The surface tension of P3HT and O-IDTBR is 21.1 and 28.1 mN m^{-1} (the contact angles are listed in Table S9, Supporting Information), respectively. Due to the lower surface tension of P3HT, it is prone to aggregate on film surface to reduce the overall free energy of blend system. As we mentioned above, the drying process of the film without TCB (stage II) is very fast, only about 10 s. Thus, only a small portion of P3HT molecules migrate to the film surface, and most of P3HT still mix with O-IDTBR, resulting in a uniform distribution along the vertical direction. While, TCB prolongs the duration of film-forming, i.e., TCB acts as plasticizer to enhance the diffusion of molecules, which provides sufficient time for molecules migrating. Hence, driven by surface energy, P3HT molecules diffuse to the top of film and O-IDTBR migrate to the bottom of the film, leading to an optimized vertical phase separation.

Consequently, we can conclude that modifying film-forming kinetics through adding cosolvent is an efficient way to increase crystallinity and optimize the lateral and vertical phase separation. While how to choose the cosolvent? Here, the study of film-forming kinetics is proposed for giving the selection criteria. First, the boiling point of cosolvent should be higher than that of the main solvent, which prolongs the self-organizing time for both components. Second, the cosolvent should have higher solubility for SMAs, thus the crystallization process of donor and acceptor can be separated, avoiding the interference with each other.

2.5. The Optimized Morphology Improves Device Performance

The photovoltaic parameters of devices based on ITO/ZnO/P3HT:O-IDTBR/MoO₃/Al are summarized in Table 2 and the corresponding current–density/voltage (J–V) curves and the

external quantum efficiency (EQE) are shown in **Figure 6**. The device fabricated without TCB shows an open circuit voltage (V_{oc}) of 0.77 V, a poor short-circuit current density (J_{sc}) of 8.81 mA cm^{-2}, a FF of 0.64, and the power conversion efficiency (PCE) is only 4.45%. After adding TCB, the corresponding device shows a PCE max of 7.18% with a V_{oc} of 0.76 V, a J_{sc} of 13.49 mA cm^{-2} and a FF of 0.70. The decreased V_{oc} is caused by the stabilization of the highest occupied molecular orbital (HOMO) due to the improved P3HT order. Generally, V_{oc} of polymer solar cells is dominated by the difference in energy levels between the HOMO of donor and the lowest unoccupied molecular orbital (LUMO) of the acceptor.[40] After adding TCB, the crystallinity of P3HT is enhanced, which results in a higher HOMO energy level of P3HT, leading to a decreased V_{oc}. Unlike V_{oc}, the J_{sc} dramatically increases to 13.49 mA cm^{-2}. The relative magnitudes of the EQE spectra correlate well with the J_{sc} values determined from the J–V curves, as shown in Figure 6B. The EQE value over the whole absorption spectra range increases greatly, indicating both P3HT and O-IDTBR have increased contribution to the J_{sc}. Usually, the improved J_{sc} is attributed to enhanced photon absorption, increased exciton dissociation and decreased bimolecular recombination.

To compare the photon absorption of devices fabricated from solution without and with TCB, we use transmission matrix optical method to calculate film-depth-dependent optical properties. Using the results shown in Figure 5, the energy dissipation Q and exciton generation rate G inside the active layer were obtained (Figure S10, Supporting Information). Under the assumption that each photon generates an exciton, which splits into one electron and hole, and the electron and hole are completely collected by electrodes. It is obvious that the calculated J_{sc} is similar, 27.51 mA cm^{-2} for the device fabricated without TCB and 27.07 mA cm^{-2} for the device fabricated with TCB. That is to say, the effect of adding TCB on photon absorption can be neglected. Hence, the improved J_{sc} is believed to be caused by the increased exciton dissociation and/or decreased bimolecular recombination.

To determine the efficiency of exciton dissociation, the curves of photogenerated current density (J_{ph}) versus effective voltage (V_{eff}) were also measured (Figure 6C).[41,42] J_{ph}
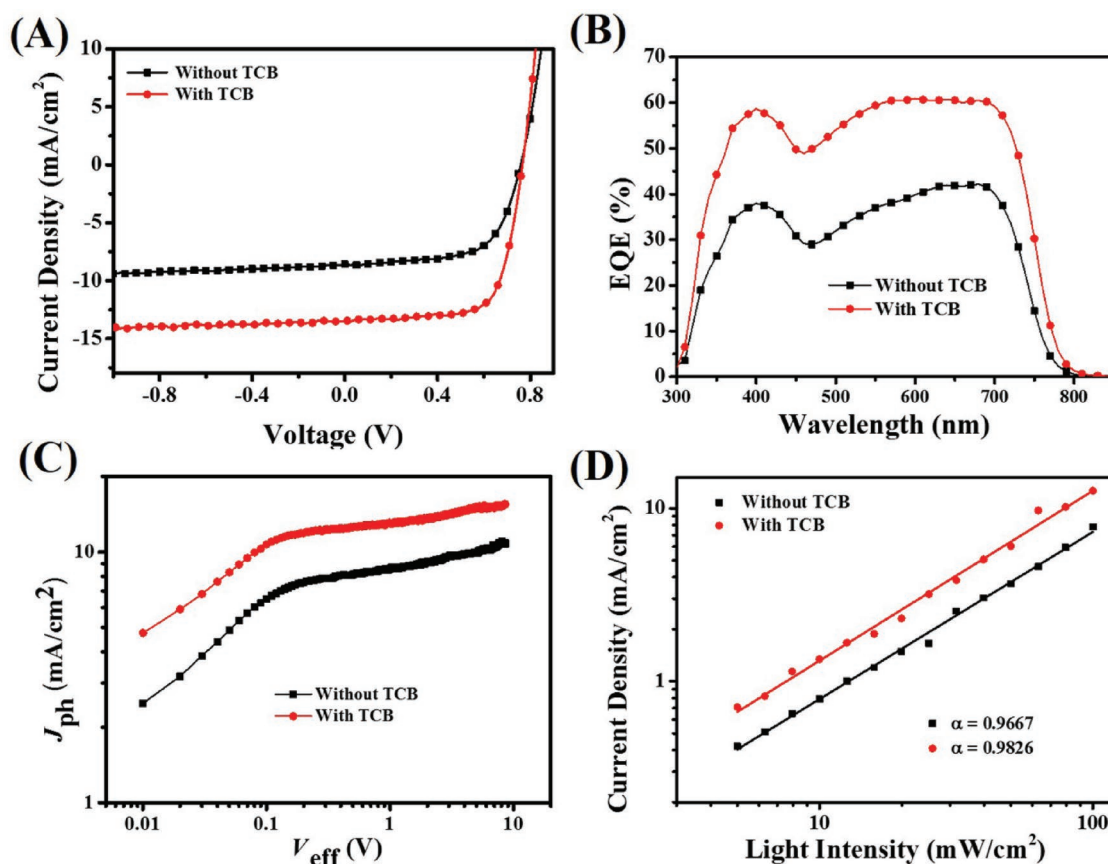
Figure 6. A) The J–V curves, B) EQE spectra, C) photocurrent density (J_{ph}) plotted with respect to effective bias (V_{eff}), dependence of D) the open-circuit voltage on light intensity for P3HT:O-IDTBR devices fabricated without and with TCB.

is defined as $J_{ph} = J_L − J_D$, where J_L and J_D represent for the photocurrent densities under light illumination and in the dark, respectively. Meanwhile, $V_{eff} = V_0 − V_a$, where V_0 is the voltage when J_{ph} equals zero and V_a is the applied voltage. V_{eff} is determined by the internal electric field in BHJ, influencing the charge-carrier transport and extraction. We observed that the J_{ph} linearly increased with increasing the voltage at a low voltage (V_{eff}) region and then became saturated at a sufficiently high value of V_{eff}, then the saturation photocurrent density (J_{sat}) could be obtained. As we mentioned above, the degree of phase separation was enhanced after the addition of TCB. Due to the short exciton lifetime, the large domain size should correspond to a small J_{sat}. Surprisingly, in our work it is obvious that the value of J_{sat} after adding TCB was significantly increased, which means the limiting factor for achieving high J_{sc} in the device devices fabricated from solution without TCB is carrier transport rather than exciton dissociation. The charge carrier collection probability (P_{coll}) was calculated by the equation $P_{coll} = J_{sc}/J_{sat}$, and it is 83.4% and 90.5% for the device fabricated from the solution without and with TCB, respectively. The increased P_{coll} suggests the easy transport and collection of carriers under short-circuit conditions. This improvement should be attributed to the formation of interpenetrating network, which provides continuous pathways for the holes and electrons. Furthermore, the enhanced crystallinity of both P3HT and O-IDTBR also improved the carrier

mobility (Table 2). Consequently, a high value of P_{coll} could be obtained after adding TCB.[43]

Another complimentary possibility for enhanced EQE is the reduced nongeminate recombination during the charge transport and extraction. The light-intensity dependencies of device performances were studied to identify the charge recombination origin in the devices. The relationship between J_{sc} and light intensity follows the relation $J_{sc} \propto P^\alpha$, where P is the light intensity and α is the exponential factor. The α factor should be 1 if there is no bimolecular recombination and it is smaller than 1 for the devices with the bimolecular charge recombination. As shown in Figure 6D, the data are plotted on a log–log scale. Both of the devices herein show a linear dependence of current density on the light intensity in logarithmic coordinates with a slope of 0.96 and 0.98 for devices fabricated without and with TCB, respectively. This indicates that bimolecular recombination is minimized due to the addition of TCB. For the active layer prepared without TCB, the coherence length of both P3HT and O-IDTBR is small (Table 1), corresponding to small crystal size, which is not good for overcoming the coulomb attraction between holes and electrons. Moreover, the low crystallinity of O-IDTBR lead to unbalanced carrier transport ($\mu_h/\mu_e = 68$) as well. Thus, the bimolecular recombination during charge transport was serious in the device. For the active layer prepared with TCB, the crystal size of both P3HT and O-IDTBR increase (Table 1), which facilitates the charge

**ADVANCED
SCIENCE NEWS**
www.advancedsciencenews.com

**ADVANCED
FUNCTIONAL
MATERIALS**
www.afm-journal.de

transport. In addition, the enhanced crystallinity of both P3HT and O-IDTBR is benefit for the formation of interpenetrating network, leading to a balanced charge transport ($\mu_h/\mu_e = 10$). Furthermore, P3HT enriches at the anode and O-IDTBR accumulates at the cathode after adding TCB, resulting in an optimized vertical phase separation. This structure could minimize the electron–hole recombination leakage at the electrode interface by providing a high energy barrier for hole/electron transport toward cathode/anode for the ITO/ZnO/P3HT:O-IDTBR/MoO$_3$/Al device structure. Owing to the reduced bimolecular recombination, a remarkable increase in FF (0.70) is obtained.

Hence, the morphology is very important for device performance based on polymer/nonfullerene blends. Hou et al. systematically comparing the P3HT/ITIC blends and poly[(4,4′-bis(2-butyloctoxycarbonyl-[2,2′-bithiophene]-5,5-diyl)-*alt*-(2,2′-bithiophene-5,5′-diyl)] (PDCBT)/ITIC blends in device performance and morphology.[44] Although the molecular energy-level alignments and optical absorption properties of both P3HT and PDCBT meet the requirements for realizing efficient PSCs, only the device based on PDCBT/ITIC shows an impressive efficiency as high as 10.16%, while the device performance based on P3HT/ITIC blends is only 1.25%. The relative low device performance was mainly attributed to the low crystallinity of both P3HT and ITIC, resulting in serious geminate and nongeminate charge recombination. Even after thermal annealing treatment, there is still no significant improvement in the morphology of P3HT/ITIC blends. From our point of view, the poor morphology of P3HT/ITIC blends originated from the weak interchain interactions of P3HT and good miscibility between P3HT and ITIC, inhibiting the crystallization of ITIC. Therefore, regulating the crystallization kinetics, in which the crystallization process of ITIC occurred prior to the one of P3HT, may be an efficient method to further optimize the morphology of P3HT/ITIC blends.

3. Conclusion

In summary, we established a straightforward relationship among film-forming kinetics, morphology, and device performance for the P3HT:O-IDTBR blend system. The film-forming kinetics of P3HT:O-IDTBR blend system was tuned through adding TCB as a cosolvent, which prolonged the film-forming duration and separated the crystallization process of P3HT and O-IDTBR since it has a higher boiling point and solubility for O-IDTBR. The separated crystallization process prevents the disturbance of each other, resulting highly crystalline film. Furthermore, we observed that the onset of P3HT aggregation occurs before L–L phase separation after adding TCB, which enables the formation of interpenetrating network. The prolonged duration of film processing permits sufficient time for O-IDTBR to migrate to the bottom and P3HT to move to the top of the film, making the inverted device structure a promising choice. The improved morphology significantly improves charge transport and suppresses bimolecular recombination, resulting in a record PCE of 7.18% for P3HT-based binary nonfullerene solar cells. Moreover, criteria for cosolvent to regulate the film-forming kinetics have been proposed: i) slower evaporation rate than the host solvent. ii) Higher solubility for

the SMAs than the host solvent. The solvent strategy outlined in this work may be transferred to other polymer:SMA blend systems. Understanding the work mechanisms of cosolvent underlying formation of phase separation structure provides straightforward approaches to optimize processing conditions of non-fullerene solar cells.

Very recently, more nonfullerene acceptor will be synthesized. Here, according to the recent researches, we try to our best to make a presumption about how to select an appropriate non-fullerene acceptor. The nonfullerene acceptor should have a complementary absorption spectrum compared with P3HT, realizing a high photon absorption efficiency. Furthermore, the energy level should also be took account, ensuring a sufficient energy offsets between P3HT and acceptor for exciton dissociation. Besides, P3HT and acceptor should have low miscibility, i.e., the difference of Flory–Huggins interaction parameters between P3HT and acceptor should be large enough. As a result, P3HT and acceptor could form relative pure phase with nanoscale, reducing the nucleation barrier, which is benefit for the crystallization and forming nano-interpenetrating network during film-forming or post annealing process.

4. Experimental Section

Materials: P3HT ($M_n = 29$ kDa, polymer dispersity index = 2.08) and O-IDTBR were purchased from Solarmer Materials Inc. CB and TCB were purchased from Sigma-Aldrich. All materials were used as received.

Characterization: The photon absorption of active layer and in situ absorption spectrum during film drying was recorded by UV–vis absorption spectroscopy (AvaLight-Hal) with halogen lamp source.

The in situ absorption spectrum was performed as following: ZnO layer was spin-coated on the top of the cleaned glass substrate. The P3HT:O-IDTBR blend solution was spread out on the substrate and spin-coated. The in situ absorption spectra were set on to record the absorption spectra immediately when spinning started with time interval of 0.5 s.

The fluorescence spectra of films were recorded using a Edinburgh fluorescence spectrometer (FLSP920).

The morphology of the active layer was investigated by TEM and atom force microscopy (AFM). TEM images were obtained from a TEM-1011 (JEOL Co., Japan) with an accelerating voltage of 100 kV. AFM images were recorded by Veeco Instruments Nanoscope in tapping mode. A silicon microcantilevel (spring constant 2 N m^{-1} and resonant frequency ≈ 70 kHz, Olympus, Japan) was used for the scanning.

The grazing incidence wide-angle X-ray scattering (GIWAXS) measurement was performed at the small and wide-angle X-ray scattering beamline at the Australian Synchrotron.[45] The detector was positioned approximately 300 mm downstream from the sample location. The precise sample-to-detector distance was determined with a silver behenate standard. 11 KeV incident X-ray with approximately a 0.25 mm × 0.1 mm spot was used to provide large enough q space. The 2D raw data were reduced and analyzed with a modified version of Nika.[46] GIWAXS patterns shown have been corrected to represent real Q_z and Q_{xy} axes with the consideration of missing wedge. Critical incident angle was determined by the maximized scattering intensity from sample scattering with negligible contribution from underneath layer scattering. All data were collected with integration time of 1 s to minimize beam damage.

Film-depth-dependent light absorption spectroscopy of photovoltaic films were performed with a home-built setup. We used low-pressure (<0 Pa) oxygen plasma to incrementally etch the film without damage of underneath film, which was monitored by a light absorption spectrometer. Upon fitting the evolution of light absorption spectra

during etching, we obtained the film-depth-dependent light absorption spectroscopy. The method is also available elsewhere.[28]

Device Fabrication and Testing: Organic solar cells were fabricated in the configuration of indium tin oxide (ITO)/ZnO/P3HT:O-IDTBR/MoO$_3$/Al. The cleaned ITO glass substrates were treated with UV-ozone for 25 min. Subsequently, ZnO layer was spin-coated on the top of the ITO glass and dried at 200 °C for 60 min. Solution with P3HT:O-IDTBR 12 mg/12 mg/mL CB with different TCB addition in volume ratio was spin-coated on the substrate to form active layer. Finally, a bilayer structure of MoO$_3$ (10 nm)/Al (100 nm) was deposited on top of the active layer by thermal evaporation in a vacuum of 2×10^{-4} Pa. The active area of single solar cell is 7.2 mm^2.

Current density–voltage (*J–V*) characteristics of the organic solar cells were measured using a computer controlled Keithley 236 source meter under AM1.5G illumination from a calibrated solar simulator with an irradiation intensity of 100 mW cm^{-2}. The EQE of the device was measured by a QE-R3011 (Enli Technology Co., Ltd.) with a lock-in amplifier at a chopping frequency of 280 Hz, and the monochromatic light was from a xenon lamp.

Supporting Information

Supporting Information is available from the Wiley Online Library or from the author.

Acknowledgements

Conflict of Interest

The authors declare no conflict of interest.

Keywords

[1] Y. Lin, J. Wang, Z.-G. Zhang, H. Bai, Y. Li, D. Zhu, X. Zhan, *Adv. Mater.* **2015**, *27*, 1170.

[2] W. Zhao, D. Qian, S. Zhang, S. Li, O. Inganäs, F. Gao, J. Hou, *Adv. Mater.* **2016**, *28*, 1706287.

[3] G. Zhang, J. Zhao, P. C. Y. Chow, K. Jiang, J. Zhang, Z. Zhu, J. Zhang, F. Huang, H. Yan, *Chem. Rev.* **2018**, *118*, 3447.

[4] X. Peng, L. Hu, F. Qin, Y. Zhou, P. K. Chu, *Adv. Mater. Interfaces* **2018**, *5*, 1701404.

[5] H. Zhang, H. Yao, J. Hou, J. Zhu, J. Zhang, W. Li, R. Yu, B. Gao, S. Zhang, J. Hou, *Adv. Mater.* **2018**, *30*, 1800613.

[6] S. Li, L. Ye, W. Zhao, H. Yan, B. Yang, D. Liu, W. Li, H. Ade, J. Hou, *J. Am. Chem. Soc.* **2018**, *140*, 7159.

[7] T. M. Clarke, J. R. Durrant, *Chem. Rev.* **2013**, *113*, 3734.

[8] Y. Huang, E. J. Kramer, A. J. Heeger, G. C. Bazan, *Chem. Rev.* **2014**, *114*, 7006.

[9] F. Zhao, C. Wang, X. Zhan, *Adv. Energy Mater.* **2018**, *8*, 1703147.

[10] S. D. Dimitrov, J. R. Durrant, *Chem. Mater.* **2014**, *26*, 616.

[11] J. Liu, J. Han, Q. Liang, J. Xin, Y. Tang, W. Ma, X. Yu, Y. Han, *ACS Omega* **2018**, *3*, 7603.

[12] Q. Liang, J. Han, C. Song, Z. Wang, J. Xin, X. Yu, Z. Xie, W. Ma, J. Liu, Y. Han, *J. Mater. Chem. C* **2017**, *5*, 6842.

[13] L. Ye, B. A. Collins, X. Jiao, J. Zhao, H. Yan, H. Ade, *Adv. Energy Mater.* **2018**, *8*, 1703058.

[14] C. Müller, T. A. M. Ferenczi, M. Campoy-Quiles, J. M. Frost, D. D. C. Bradley, P. Smith, N. Stingelin-Stutzmann, J. Nelson, *Adv. Mater.* **2008**, *20*, 3510.

[15] C.-W. Chu, H. Yang, W.-J. Hou, J. Huang, G. Li, Y. Yang, *Appl. Phys. Lett.* **2008**, *92*, 103306.

[16] X. Yang, J. Loos, S. C. Veenstra, W. J. H. Verhees, M. M. Wienk, J. M. Kroon, M. A. J. Michels, R. A. J. Janssen, *Nano Lett.* **2005**, *5*, 579.

[17] A. J. Moulé, K. Meerholz, *Adv. Mater.* **2008**, *20*, 240.

[18] J. Liu, L. Chen, B. Gao, X. Cao, Y. Han, Z. Xie, L. Wang, *J. Mater. Chem. A* **2013**, *1*, 6126.

[19] F. Padinger, R. S. Rittberger, N. S. Sariciftci, *Adv. Funct. Mater.* **2003**, *13*, 85.

[20] J. Vogelsang, J. M. Lupton, *J. Phys. Chem. Lett.* **2012**, *3*, 1503.

[21] S. R. Cowan, N. Banerji, W. L. Leong, A. J. Heeger, *Adv. Funct. Mater.* **2012**, *22*, 1116.

[22] S. Holliday, R. S. Ashraf, A. Wadsworth, D. Baran, S. A. Yousaf, C. B. Nielsen, C.-H. Tan, S. D. Dimitrov, Z. Shang, N. Gasparini, M. Alamoudi, F. Laquai, C. J. Brabec, A. Salleo, J. R. Durrant, I. McCulloch, *Nat. Commun.* **2016**, *7*, 11585.

[23] A. M. Nardes, A. J. Ferguson, P. Wolfer, K. Gui, P. L. Burn, P. Meredith, N. Kopidakis, *ChemPhysChem* **2014**, *15*, 1539.

[24] Q. Liang, J. Han, C. Song, J. Xin, X. Yu, Z. Xie, D.-M. Smilgies, K. Zhao, J. Liu, Y. Han, *J. Mater. Chem. A* **2018**, *6*, 15610.

[25] W. Ma, C. Yang, X. Gong, K. Lee, A. J. Heeger, *Adv. Funct. Mater.* **2005**, *15*, 1617.

[26] X. Li, J. Yao, I. Angunawela, C. Sun, L. Xue, A. Liebman-Pelaez, C. Zhu, C. Yang, Z.-G. Zhang, H. Ade, Y. Li, *Adv. Energy Mater.* **2018**, *8*, 1800815.

[27] W. Zhao, S. Li, H. Yao, S. Zhang, Y. Zhang, B. Yang, J. Hou, *J. Am. Chem. Soc.* **2017**, *139*, 7148.

[28] Y. Zhang, D. Deng, Z. Wang, Y. Wang, J. Zhang, J. Fang, Y. Yang, G. Lu, W. Ma, Z. Wei, *Adv. Energy Mater.* **2017**, *7*, 1701548.

[29] B. Schmidt-Hansberg, M. Sanyal, M. F. G. Klein, M. Pfaff, N. Schnabel, S. Jaiser, A. Vorobiev, E. Müller, A. Colsmann, P. Scharfer, D. Gerthsen, U. Lemmer, E. Barrena, W. Schabel, *ACS Nano* **2011**, *5*, 8579.

[30] J. J. van Franeker, M. Turbiez, W. Li, M. M. Wienk, R. A. Janssen, *Nat. Commun.* **2015**, *6*, 6229.

[31] J. Liu, S. Shao, H. Wang, K. Zhao, L. Xue, X. Gao, Z. Xie, Y. Han, *Org. Electron.* **2010**, *11*, 775.

[32] N. S. Güldal, T. Kassar, M. Berlinghof, T. Unruh, C. J. Brabec, *J. Mater. Res.* **2017**, *32*, 1855.

[33] N. Shin, L. J. Richter, A. A. Herzing, R. J. Kline, D. M. DeLongchamp, *Adv. Energy Mater.* **2013**, *3*, 938.

[34] B. A. Collins, Z. Li, C. R. McNeill, H. Ade, *Macromolecules* **2011**, *44*, 9747.

[35] F. C. Spano, *Acc. Chem. Res.* **2010**, *43*, 429.

[36] J. L. Hernandez, N. Deb, R. M. W. Wolfe, C. K. Lo, S. Engmann, L. J. Richter, J. R. Reynolds, *J. Mater. Chem. A* **2017**, *5*, 20687.

[37] G. Reiter, *Chem. Soc. Rev.* **2014**, *43*, 2055.

**ADVANCED
SCIENCE NEWS**

www.advancedsciencenews.com

**ADVANCED
FUNCTIONAL
MATERIALS**

www.afm-journal.de

[38] L. Bu, S. Gao, W. Wang, L. Zhou, S. Feng, X. Chen, D. Yu, S. Li, G. Lu, *Adv. Electron. Mater.* **2016**, *2*, 1600359.

[39] G. Lu, R. D. Pietro, L. S. Kölln, I. Nasrallah, L. Zhou, S. Mollinger, S. Himmelberger, N. Koch, A. Salleo, D. Neher, *Adv. Electron. Mater.* **2016**, *2*, 1600267.

[40] S. Sweetnam, K. R. Graham, G. O. N. Ndjawa, T. Heumüller, J. A. Bartelt, T. M. Burke, W. Li, W. You, A. Amassian, M. D. McGehee, *J. Am. Chem. Soc.* **2014**, *136*, 14078.

[41] J.-L. Wu, F.-C. Chen, Y.-S. Hsiao, F.-C. Chien, P. Chen, C.-H. Kuo, M. H. Huang, C.-S. Hsu, *ACS Nano* **2011**, *5*, 959.

[42] A. K. K. Kyaw, D. H. Wang, V. Gupta, W. L. Leong, L. Ke, G. C. Bazan, A. J. Heeger, *ACS Nano* **2013**, *7*, 4569.

[43] T. M. Clarke, A. M. Ballantyne, J. Nelson, D. D. C. Bradley, J. R. Durrant, *Adv. Funct. Mater.* **2008**, *18*, 4029.

[44] Y. Qin, M. A. Uddin, Y. Chen, B. Jang, K. Zhao, Z. Zheng, R. Yu, T. Joo, S. Han, Y. Woo, J. Hou, *Adv. Mater.* **2016**, *28*, 9416.

[45] N. M. Kirby, S. T. Mudie, A. M. Hawley, D. J. Cookson, H. D. T. Mertens, N. Cowieson, V. Samardzic-Boban, *J. Appl. Crystallogr.* **2013**, *46*, 1670.

[46] J. Ilavsky, *J. Appl. Crystallogr.* **2012**, *45*, 324.

1807591 (12 of 12)